Journal of the European Ceramic Society 44 (2024) 2744–2753

Contents lists available at ScienceDirect

Journal of the European Ceramic Society

journal homepage: www.elsevier.com/locate/jeurceramsoc

Cold sintering of $BaZr_{0.8}Y_{0.2}O_{3-\delta}$ ceramics: Phase formation and grain boundary properties

Moritz Kindelmann [a,b,c,*], Julian N. Ebert [c], Dylan Jennings [c], Doris Sebold [c], Wolfgang Rheinheimer [c,d], Martin Bram [c], Joachim Mayer [a,b], Olivier Guillon [c,e]

[a] Forschungszentrum Jülich GmbH Ernst Ruska-Centre for Microscopy and Spectroscopy with Electrons (ER-C), 52425 Jülich, Germany
[b] RWTH Aachen University, Central Facility for Electron Microscopy (GFE), 52074 Aachen, Germany
[c] Forschungszentrum Jülich GmbH, Institute of Energy and Climate Research, Materials Synthesis and Processing (IEK-1), 52425 Jülich, Germany
[d] University of Stuttgart, Institute for Manufacturing Technologies of Ceramic Components and Composites (IFKB), 70569 Stuttgart, Germany
[e] Jülich Aachen Research Alliance, JARA-Energy, 52425 Jülich, Germany

ARTICLE INFO

Keywords:
Cold Sintering
Sintering
Protonic Ceramics
Grain boundaries
BaZrO3

ABSTRACT

Electrochemical devices based on the proton conducting ceramic $BaZrO_3$ have shown their immense potential for efficient energy conversion and gas separation processes at intermediate temperatures. A major drawback of this material class is the inevitably high sintering temperature, which is necessary to reach sufficient densities for gas tightness. Recently, cold sintering has been applied to densify $BaZrO_3$ – $BaCeO_3$ solid solutions at low temperatures using a partial dissolution of the Ce-rich phase. Here, we apply the method to $BaZr_{0.8}Y_{0.2}O_{3-\delta}$ (BZY20), which is a Ce-free proton conducting ceramic. We show that densification by cold sintering is viable at temperatures between 150 °C and 250 °C under uniaxial pressures of 400 MPa and deionized water as a sintering aid. The dissolution of yttrium from BZY20 during cold sintering acts as the trigger for densification at low temperatures but forms $Y(OH)_3$ as an instable side product. Therefore, we developed a two-step cold sintering process that adds an additional thermal treatment between 900 and 1100 °C directly after the cold sintering process to enable electrochemical characterization and transmission electron microscopy investigations.

1. Introduction

Proton conducting ceramics have shown a large potential for the defossilization of future energy systems based on renewable energy sources due to their reversible and robust performance in fuel cell and electrolyser applications [1]. Recent developments show the immense potential of proton-conducting fuel and electrolysis cells [2–7] and membrane reactors [8–11] for electrochemical conversion and separation processes. In general, ceramic proton conducting cells and reactors are based on the perovskite ceramic $BaZrO_3$, which is usually doped with trivalent cations (Y^{3+}, Sc^{3+}, Yb^{3+}), which act as acceptor dopants. Most material designs use yttrium in the range between 10–20 mol% to generate oxygen ion vacancies, which allow the hydration of the material through the dissociative adsorption of water at intermediate temperatures [12].

Compared to highly conductive proton conductors based on solid solutions of the perovskites $BaZrO_3$ and $BaCeO_3$ (BZCY) [13,14], Y doped $BaZrO_3$ (BZY) does not suffer from instability issues in contact with H_2O and CO_2 under applied operation conditions [15–17]. However, $BaZrO_3$ based ceramics suffer from their intrinsic refractory properties, making high sintering temperatures around 1600 °C inevitable to manufacture gas tight membranes and electrolytes. The sintering temperatures can be slightly reduced (to around 1500 °C) through the application of sintering aids as ZnO, CoO, or NiO, which facilitate a low-cost, one-step solid state reactive sintering (SSRS) procedure [18–21]. However, the introduction of sintering aids leads to negative side effects, such as the formation of secondary phases [22,23], grain boundary segregation phenomena [24,25] and reduced proton uptake induced by lower effective acceptor dopant concentrations [26]. Because of that, the removal of performance degrading sintering aids as well as a further reduction of the processing temperatures of $BaZrO_3$ based ceramics are of high interest [27]. This could decrease the overall energy consumption during manufacturing of proton conducting ceramic components and open up new material combinations and co-sintering approaches (e.g. metal supported electrochemical cells) [28–30].

---

* Corresponding author at: Forschungszentrum Jülich GmbH Ernst Ruska-Centre for Microscopy and Spectroscopy with Electrons (ER-C), 52425 Jülich, Germany.
E-mail address: m.kindelmann@fz-juelich.de (M. Kindelmann).

https://doi.org/10.1016/j.jeurceramsoc.2023.12.060
Received 15 September 2023; Received in revised form 24 November 2023; Accepted 14 December 2023

A novel approach to drastically lower the sintering temperature of ceramic materials is the cold sintering process (CSP) recently developed by Randall et al. [31]. Liquid sintering aids and high mechanical pressures are combined to trigger pressure solution processes, allowing densification at temperatures below 400 °C [31,32]. A broad variety of ceramic materials (e.g. ZnO [33–35], $BaTiO_3$ [36,37], CeO_2 [38,39] and LLZO [40,41]) has been densified using CSP at strongly decreased processing temperatures. Recently, we reported on the cold sintering of a $BaZrO_3$ – $BaCeO_3$ solid solution ($BaZr_{0.7}Ce_{0.2}Y_{0.1}O_{3-\delta}$, BZCY72), where a partial dissolution of the Ce-rich perovskite in water acted as the trigger for densification [42,43]. In the following we transferred the gained knowledge to a system that does not contain Ce, to elaborate alternative pathways to trigger the densification through cold sintering.

Here, we investigate the cold sintering of BZY20 ceramics using a one-step as well as a two-step cold sintering approach using deionized water as a sintering additive. At a maximum temperature of 250 °C and 400 MPa, BZY20 powders can be densified to relative densities around 87%. However, the formation of unstable side products during the cold sintering process complicates further characterization by high-resolution electron microscopy and electrochemical investigations. Therefore, we developed a two-step cold sintering procedure, which utilizes the advantages of high strength molybdenum (TZM) tools in a field assisted sintering/spark plasma sintering (FAST/SPS) apparatus. The combination of a cold sintering step at 250 °C with a subsequent thermal treatment at 900 to 1100 °C in the same tool allows us to remove unstable reaction products, increase the relative density to over 90%, facilitating the characterization of the electrochemical performance as well as the grain boundary properties. As the sample is not removed from the pressing tool, the overall processing time can be kept below one hour. Here, we applied electrochemical impedance spectroscopy (EIS) and high-resolution scanning transmission electron microscopy (HR-STEM) to investigate the proton conductivity and couple it to the grain boundary structure and chemistry.

2. Experimental methods

2.1. Powder synthesis and cold sintering

In the following, ceramic powders with a nominal composition of $BaZr_{0.8}Y_{0.2}O_{3-\delta}$ (BZY20) were used. The powder synthesis is based on a mixed oxide route. The powder precursors $BaCO_3$, ZrO_2, and Y_2O_3 (Sigma-Aldrich), were milled in isopropanol using a planetary ball mill (Retsch PM400, Germany) using a zirconia jar and milling balls to decrease and homogenize the pre-calcination particle distribution. Afterwards, calcination of the powders was done at 1175 °C for 3 h in air. After calcination the powders were sieved to remove large agglomerates. As reference, $BaZrO_{3-\delta}$ (BZO) was synthesized from $BaCO_3$ and ZrO_2 using the same processing parameters. Details on the powder preparation can be found elsewhere [44,45].

The cold sintering experiments were carried out in a field-assisted sintering technology/spark plasma sintering machine (FAST/SPS, FCT Systeme HP-D5, Germany) utilizing a TZM die set-up (TZM = Mo-based alloy from Plansee SE, Austria) with a diameter of 12 mm. The die was filled with 4 g BZY20 powder, and 5 wt% deionized water was homogeneously dripped onto the green body using a micropipette (Eppendorf, Germany). The powder was compacted at temperatures from 150 °C to 250 °C (in 50 °C steps) using a uniaxial pressure of 400 MPa, a heating rate of 20 K/min, and a heating time of between 10 and 60 min. This procedure will be called one-step cold sintering. Additionally, a two-step cold sintering procedure was developed that combines cold sintering at 250 °C for 10 min with different thermal post-treatments between 900 – 1100 °C, which are made directly after cold sintering in the same tool setup. The uniaxial pressure was decreased to 100 MPa to prevent high temperature creep of the TZM tools and a heating rate of 50 K/min and a heating time of 5 min was applied. The processing cycles are visualized in Fig. 1 for clarification. After cooling inside of the FAST/SPS chamber the samples were demolded and residual carbon paper was removed by dry grinding.

As reference for electrochemical characterization, the BZY20 powder was uniaxially pressed at 25 MPa for 1 min, afterwards cold isostatically pressed at 400 MPa for 2 min and then sintered at 1600 °C for 24 h in a BZY20 powder bed.

2.2. Density, phase analysis and scanning electron microscopy

The relative density of all sintered samples was determined by the Archimedes method. One-step cold sintered samples were measured in heptane instead of deionized water due to the high reactivity of secondary phases formed during cold sintering with water. Two-step cold sintered samples were measured in deionized water. X-ray diffraction (XRD, Brucker D4 Endeavor, USA) was used to investigate the phase composition of starting powders, one-step and two-step cold sintered samples. Additionally, the morphology of powders (Supplementary Fig. S1) and the microstructure of sintered samples were characterized by scanning electron microscopy (SEM, Zeiss FEG-GeminiSEM 450, Germany).

2.3. Transmission electron microscopy

To investigate the microstructure of two-step cold sintered samples and the chemical composition and structure at grain boundaries, electron transparent lamellae were cut from a representative area using

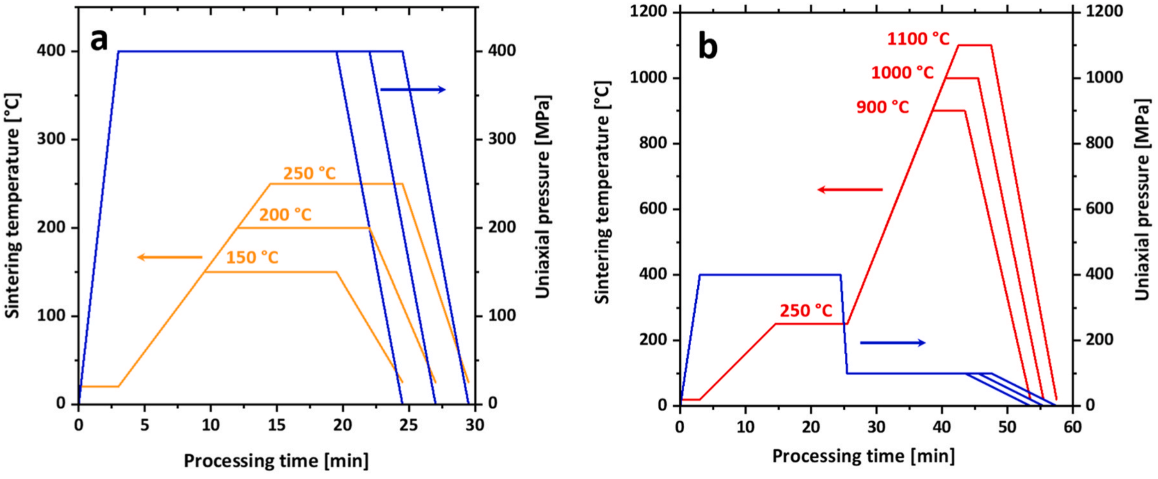

Fig. 1. Processing cycles of one-step cold sintering (a) and two-step cold sintering experiments (b).

focused ion beam SEM (FIB-SEM, FEI Helios NanoLab 460F1, USA). Scanning transmission electron microscopy (STEM) was performed at 200 kV using a probe corrected TFS Spectra 300 microscope (Thermo Fischer Scientific, USA), which is equipped with a Super-X EDS detector. High resolution transmission electron microscopy (HRTEM) was performed at 300 kV using an image corrected FEI Titan 80–300 TEM which is equipped with a C_S-corrector (CEOS CETCOR).

2.4. Electrochemical characterization

Electrochemical impedance spectroscopy (EIS) was used to compare the conductivity of two-step cold sintered BZY20 ceramics to a conventionally processed BZY20 sample made from the same starting powder. To clearly separate bulk and grain boundary conductivity the impedance was measured between 600 and 150 °C using an Alpha-A High Performance Frequency Analyzer, (Novocontrol, Germany) in the frequency range of 10 MHz to 0.1 Hz in wet Ar/2.9%H_2 ($p(H_2O)$ ~0.025 bar). The impedance data was analyzed using an equivalent circuit consisting of a series of parallel resistance and constant phase elements (R||CPE) according to the brick layer model [46,47] in RelaxIS3 (version 3.0.20.19, rhd instruments, Germany). The R||CPE elements were attributed to bulk, grain boundary or electrode by calculating the corresponding capacity [44,47,48]. Subsequently, the total, bulk and effective grain boundary conductivity are calculated using Eqs. (1–3), respectively. In the given equations R_b and R_{gb} are the resistivities derived from the fitting and l and A are the thickness and area of the measured sample.

$$\sigma_t = \frac{1}{(R_b + R_{gb})}\frac{l}{A} \tag{1}$$

$$\sigma_b = \frac{1}{R_b}\frac{l}{A} \tag{2}$$

$$\sigma_{eff.gb} = \frac{1}{R_{gb}}\frac{l}{A} \tag{3}$$

3. Results and discussion

3.1. Microstructure and phase formation during cold sintering of BZY20

In first section, we discuss the densification and phase formation during single and two-step cold sintering. The densification, microstructure, and phase formation of BZY20 samples were investigated, and the sintering experiments were carried out in a parameter range of 150 °C to 250 °C (50 K steps) for 10, 30, and 60 min at 400 MPa, using deionized water as a sintering aid.

The relative densities of the sintered pellets are shown in Fig. 2a. It can be observed that sintering temperatures of 150 °C achieved relative densities around 80%. However, with an increase in temperature to 200 °C and 250 °C, higher densities between 85% to 87% were obtained. Microstructural analysis of the fractured surfaces, as shown in Fig. 2(b-e), revealed a fine-grained structure with a notable amount of residual porosity. Some of the small crystallites are embedded in an amorphous secondary phase (as shown later by TEM investigations), which is highlighted by red circles. Comparable microstructural features were reported for the cold sintered Ce-containing proton conductor BZCY ($BaZr_{0.7}Ce_{0.2}Y_{0.1}O_{3-\delta}$) and attributed to the formation of secondary phases through solution processes [42,43].

Fig. 3 displays XRD diffractograms focusing on 2Θ values between 15° and 26°, which correspond to the (110) and (020) diffraction peaks of $BaCO_3$ and the (100) peaks of $Y(OH)_3$, as well as 2Θ values between 26° and 33°, representing the (110) diffraction peak of $BaZrO_3$ and Y_2O_3. The XRD analysis clearly indicates that the starting powder contained residual $BaCO_3$ and Y_2O_3 that were not completely decomposed during the low-temperature calcination process at 1175 °C. After cold sintering at 150 °C and short dwell times (10 and 30 min), no apparent changes in the phase composition can be observed.

However, after heating to 150 °C for 1 h, and for all samples sintered at temperatures above 150 °C, an additional peak at $2\Theta = 6°$ becomes visible, which can be attributed to the (100) peak of $Y(OH)_3$. The appearance of $Y(OH)_3$ in the XRD patterns correlates with the higher relative density values observed in Fig. 2(a). The increased temperatures and dwell times during sintering may cause an increased dissolution of Y, either from the BZY20 powder particles or Y_2O_3 residuals. The observable hydrothermal dissolution process, which leads to the formation of $Y(OH)_3$, is assumed to aid densification by allowing particle sliding and a better rearrangement under high mechanical pressure.

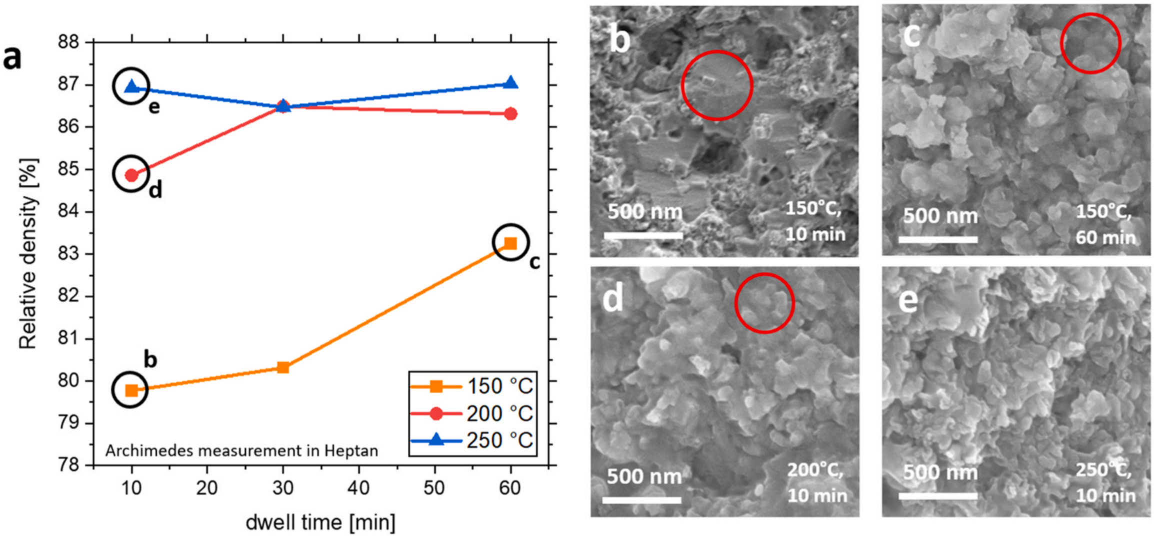

Fig. 2. Influence of sintering temperature and dwell time on the relative density and microstructure of BZY20 ceramics. (a) Relative density of cold sintered BZY20 measured by Archimedes method in heptane. (b-e) SEM images of the fracture surfaces of selected samples 150 °C, 10 min (b), 150 °C, 60 min (c), 200 °C, 10 min (d) and 250 °C, 10 min (e). The measured density of the SEM is highlighted in (a) as black circles. Additionally, red circles highlight the formation of an amorphous secondary phase.

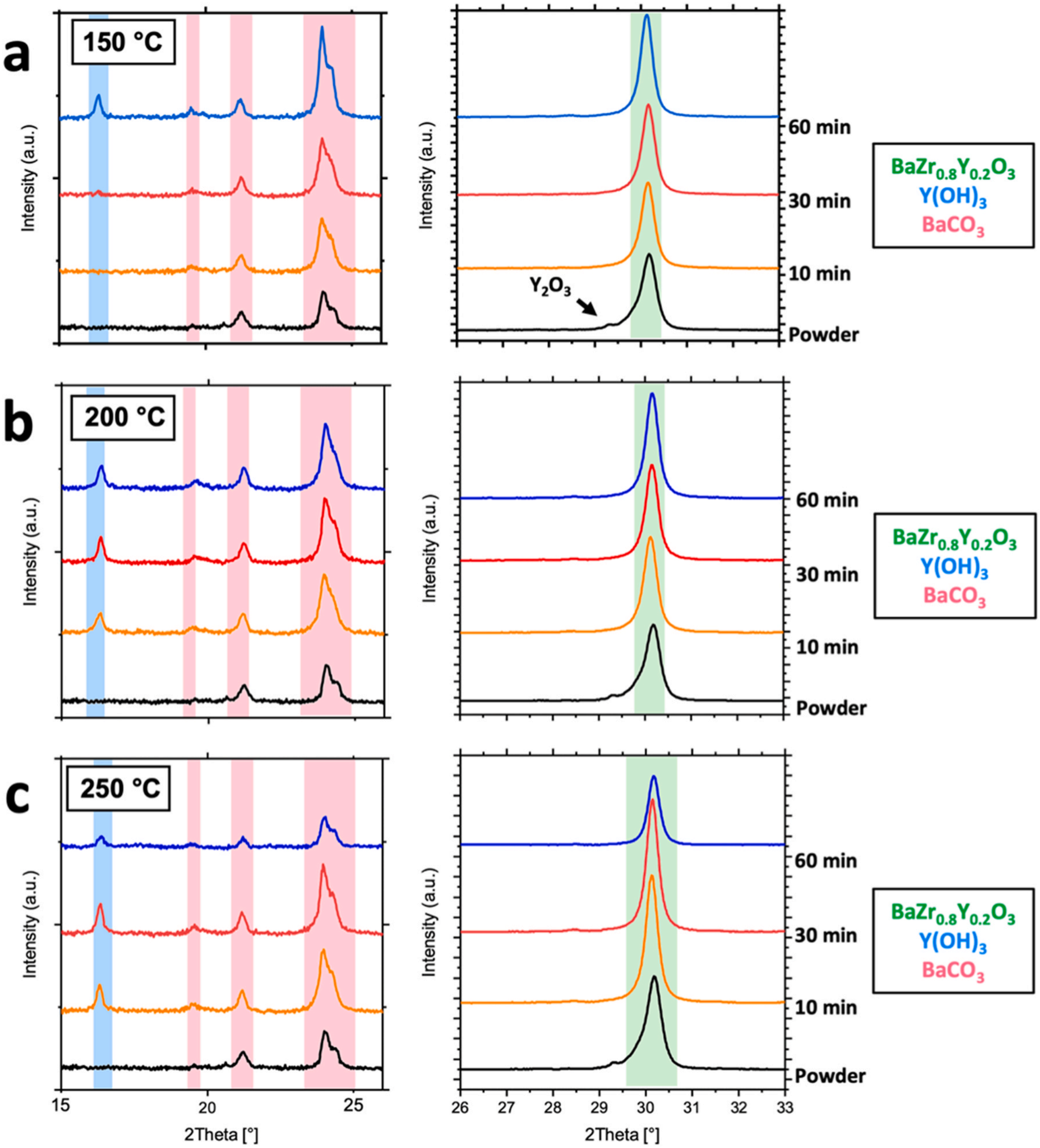

Fig. 3. Phase formation during cold sintering at varied sintering temperatures and dwell times. XRD diffractograms between 2θ = 15–26° and 26–33° with different magnifications to highlight the secondary phases as well as the main phases. The sintering temperature is increased from top to bottom from 150 °C (a), 200 °C (b) to 250 °C (c).

For a more comprehensive understanding of the phase composition and microstructure, additional characterization was performed using SEM-EDS, as depicted in Fig. 4. The polished cross-section (Fig. 4a) of the cold-sintered BZY20 densified at 250 °C and 400 MPa exhibits a heterogeneous microstructure, revealing the presence of residual pores and different secondary phases. Using the EDS mappings of the major components (Fig. 4b-d), it is possible to identify various secondary phases resulting from hydrothermal dissolution processes that occurred during cold sintering. EDS point scan were derived from specific areas in the mapping to elucidate the composition of distinct phases (Fig. 4e, f): the primary bulk phase (1), a phase enriched in zirconium and depleted in barium (2), and a phase rich in yttrium (3). Comparing the SEM-EDS results to the phase composition of the cold-sintered samples determined by XRD, the Y rich phase can be attributed to $Y(OH)_3$, which is a product of the dissolution process during cold sintering. However, the presence of a Zr rich and Ba deficient phase could not be detected by XRD, likely due to a low total amount in the sample. The phase changes during cold sintering observed by SEM and XRD clearly highlight that dissolution of Y containing particles is the major driving factor for densification of BZY20, as already observed for Ce containing BZCY ceramics [42,43].

Further evidence for the dominant role of Y during cold sintering can be derived from the densification behavior of pure $BaZrO_3$ (BZO) powders that were prepared using the same powder processing route. Even though residual $BaCO_3$ is present due to low calcination temperatures, no cold sintering activity can be observed (Fig. 5a), excluding $BaCO_3$ as a dominant factor facilitating densification during cold sintering. A direct comparison between the densification behavior is displayed in Fig. 5a. During the application of uniaxial pressure (marked with blue background) both powders show a similar compaction behavior, which is likely the elastic response of the setup and a powder compaction due to

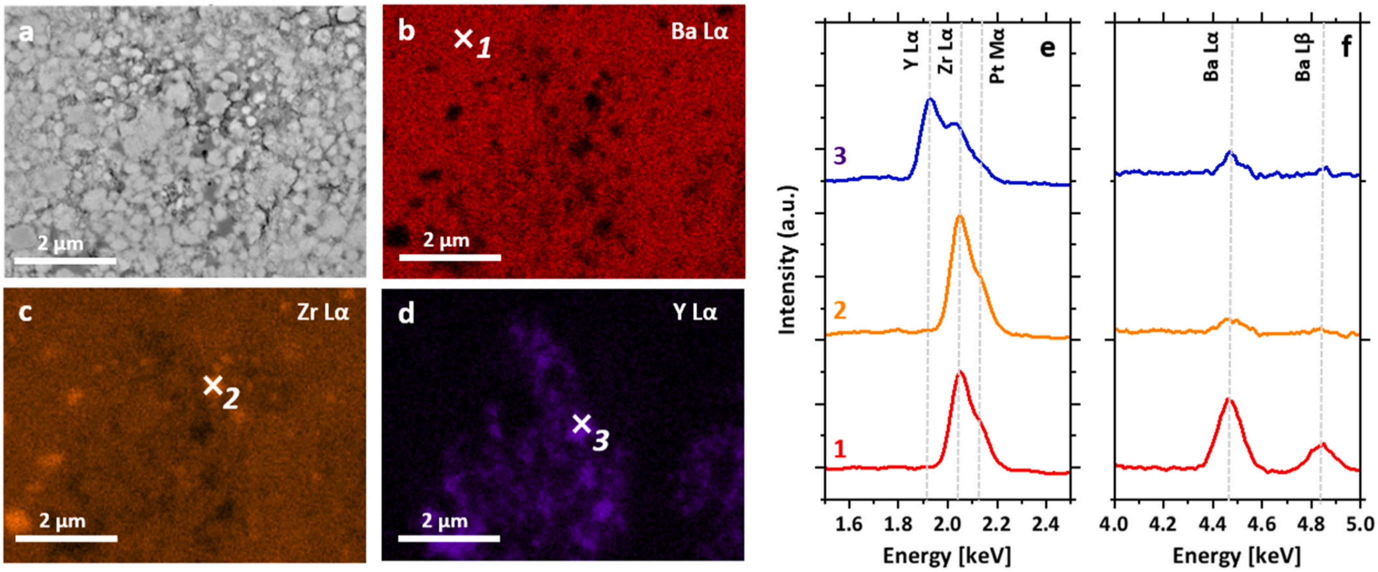

Fig. 4. Microstructure after cold sintering of BZY20 at 250 °C using 400 MPa for 10 min (a) SEM image of a polished cross section showing the heterogeneous microstructure. (b-d) SEM-EDS mappings of the major components of BZY20. (e, f) Selected EDS spectra in the energy range of the Y Lα, Zr Lα and Pt Mα peaks (e) as well as the Ba Lα,Lβ peaks (f). All spectra were derived from the spectral images in b-d.

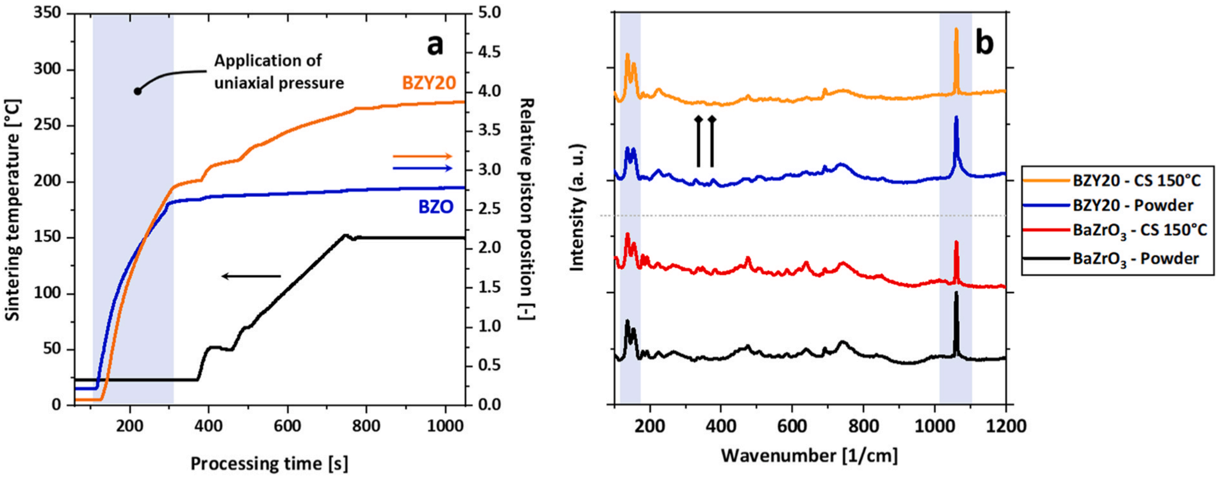

Fig. 5. Comparison of the cold sintering behavior between BZY20 and undoped $BaZrO_3$ (a) Sintering curves of BZO and BZY20 sintered at 150 °C under a uniaxial pressure of 400 MPa using deionized H_2O as a sintering aid. (b) Raman spectroscopy measurements of powders and cold sintered samples. Blue background highlights the vibrational modes associated with $BaCO_3$. In BZY20 the Y-O vibrational modes (◆) are reduced after cold sintering.

the loading. Once heat is applied, a clear piston displacement is already measurable for BZY20 powders even at low temperatures of 150 °C, while BZO powders show no sign of powder densification. Additionally, Raman measurements on both starting powders and cold sintered samples give an insight into the phase changes induced by cold sintering (Fig. 5b). It is clearly visible that both powders as well as the sintered samples contain $BaCO_3$ (highlighted by blue background). Furthermore, the Raman spectrum of BZO samples is not affected by the cold sintering treatment, while in BZY20 small changes in the Y-O vibrational modes are visible.

Even though a substantial densification could be achieved in one-step cold sintering, the presence of unstable phases after sintering prevents electrochemical characterization and high-resolution electron microscopy. Therefore, a two-step sintering procedure was developed (Fig. 1b) to remove instable components ($Y(OH)_3$) as well as to further increase the relative density. Fig. 6 summarizes the effect of a second sintering step at higher temperatures on the relative densities and the phase composition. The two-step cold sintering process yields relative densities between 91% and 95% (Fig. 6a), which is significantly higher than after one-step cold sintering. Furthermore, the XRD diffractograms in Fig. 6b, c clearly show the removal of the instable secondary phase Y $(OH)_3$ that was present after cold sintering at 250 °C. All temperatures used here are above the decomposition temperature of $Y(OH)_3$ into Y_2O_3 and H_2O [49,50]. However, the temperatures are not sufficient to decompose residual $BaCO_3$, which remains inside the samples [51]. This treatment not only stabilizes the cold sintered samples in contact with wet atmosphere but also allows high resolution investigation of the microstructures and grain boundaries by transmission electron microscopy and a detailed electrochemical characterization.

3.2. *Grain boundary composition and resulting electrochemical properties*

In the following section, the electrochemical properties are investigated and high-resolution electron microscopy is used to correlate the bulk properties to the microstructure and the chemical composition at the grain boundaries.

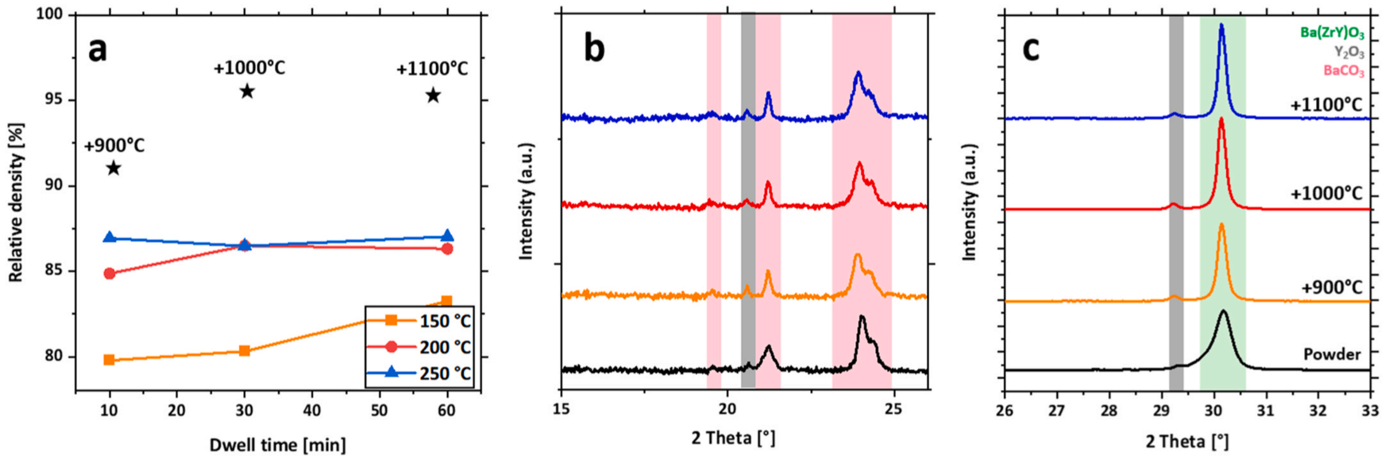

Fig. 6. Densification and phase formation after two-step cold sintering. (a) Relative density measured in deionized water (stars), compared to the relative density after cold sintering (Fig. 2a) (b, c) XRD diffractograms of the starting powder and two-step cold sintered BZY20.

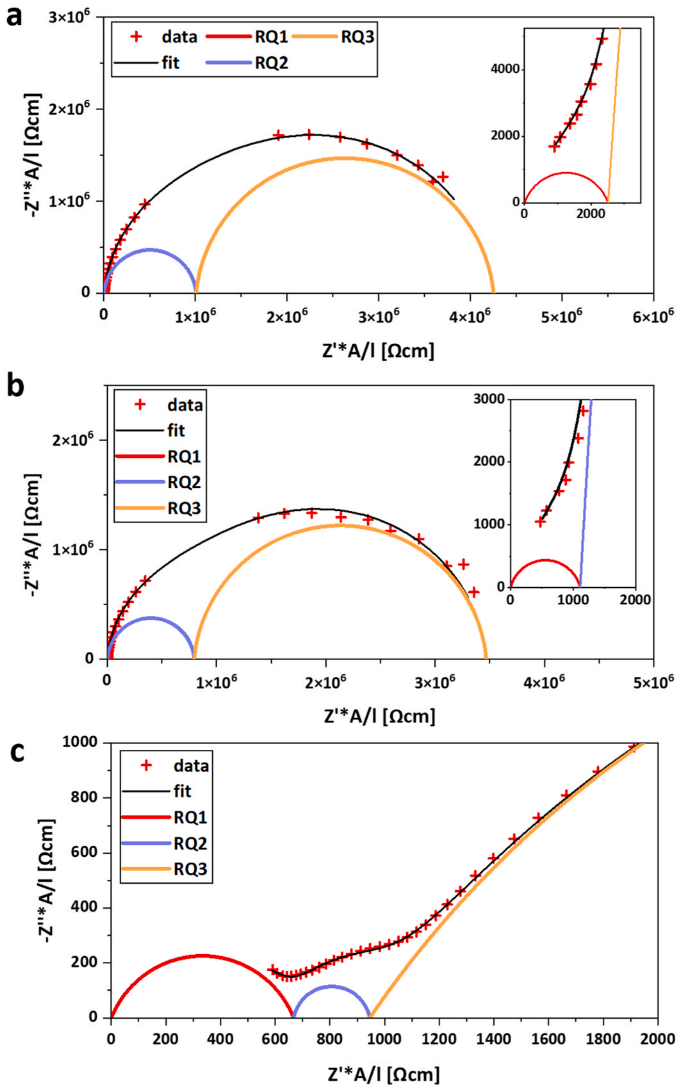

Fig. 7. Nyquist plots of electrochemical impedance spectroscopy measurements at 300 °C in wet Ar/H_2. of two-step cold sintered BZY20 (a) 900 °C, (b) 1100 °C and conventionally sintered BZY20 (1600 °C, 24 h) (c). The semicircles below the measurement data represent the RQ circuits used for fitting. RQ1 corresponds to the bulk, RQ2 to the grain boundary and RQ3 to the electrode contribution.

Figs. 7 and 8 show the electrochemical impedance spectroscopy (EIS) measurements to assess the conductivity of two-step cold sintered BZY20. We used a conventionally processed BZY20 sample, which was sintered in a BZY20 sacrificial powder bed at 1600 °C for 24 h in air as a reference [44]. Firstly, Fig. 7 displays three Nyquist plots of EIS measurements at 300 °C in wet Ar/H_2. Comparing the different contributions of bulk (RQ1), grain boundary (RQ2) and electrode (RQ3) it becomes clear that both cold sintered samples (Fig. 7a and b) have a very high grain boundary resistivity that is dominating the overall conductivity. A comparison with the conventionally processed sample (Fig. 7c) highlights the strong differences. Here, the grain boundary resistivity is smaller compared to the bulk resistivity, an effect recently highlighted by Ebert et al. [44].

The presented fitting procedure is applied between temperatures of 150 and 600 °C. The conductivity is displayed separately in the total, bulk and effective grain boundary conductivity, which are represented as squares, circles and triangles in Fig. 8. The conductivity values are derived from the fitting procedure using Eqs. (1–3) [52]. The total conductivity of both cold sintered samples (900 and 1100 °C) is several orders of magnitude lower than the conductivity of the conventionally processed reference specimen.

This stems from the large difference in effective grain boundary conductivity between cold and conventionally sintered samples (highlighted by arrows in the graph). When comparing the bulk conductivity, all tested samples are in the same conductivity range. The extremely low grain boundary conductivity observed in impedance measurements might be explained by the presence of the secondary phases and grain boundary films being present between BZY grains. Additionally, the extremely small grain size of cold sintered samples increases the impact of the grain boundary conductivity on the total performance.

Therefore, an in-depth characterization of the microstructure and the grain boundary composition is needed to correlate the conductivity results to distinct microstructural features. Fig. 9 shows a TEM-EDS mapping for two-step cold sintered BZY20 (250 °C for 10 min at 400 MPa followed by 1100 °C for 5 min at 100 MPa) on the microstructure and grain boundary scale. The microstructure is characterized by a very small grain size and secondary phases that are predominantly located at triple points (Fig. 9b) and in between grains (Fig. 9a). In addition to the major components of BZY20 (Ba, Zr, Y and O), Fig. 9a also includes Carbon, which can be associated to residual $BaCO_3$ (also clearly present in XRD and Raman measurements).

A clear separation between the crystalline BZY20 grains and the secondary phase inclusion can be observed. The secondary inclusion can be separated into two distinct phases: a carbon-rich phase, most likely identified as $BaCO_3$, and an yttrium-rich phase, presumably originating

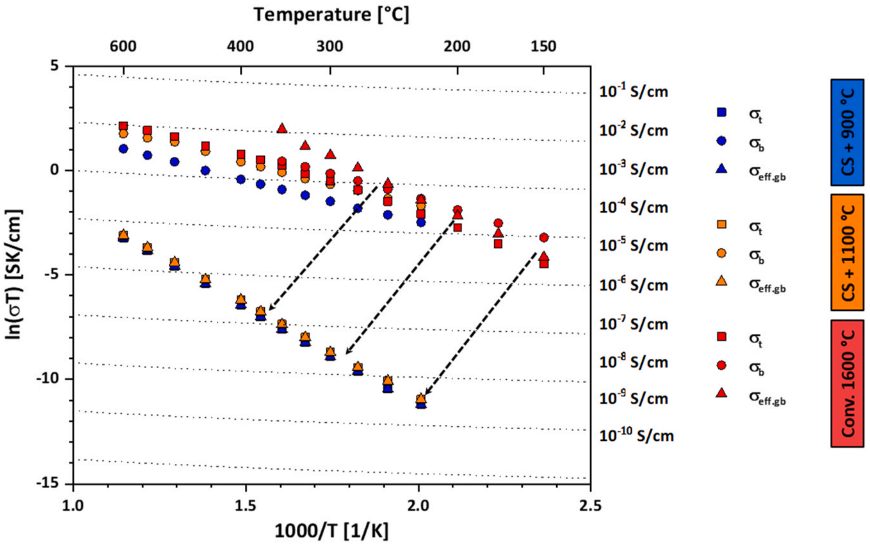

Fig. 8. Arrhenius plot of the total, bulk, and effective grain boundary conductivity of conventionally sintered BZY20 (1600 °C, 24 h) and two-step cold sintered BZY20 (900 °C / 1100 °C) measured in wet Ar/H_2.

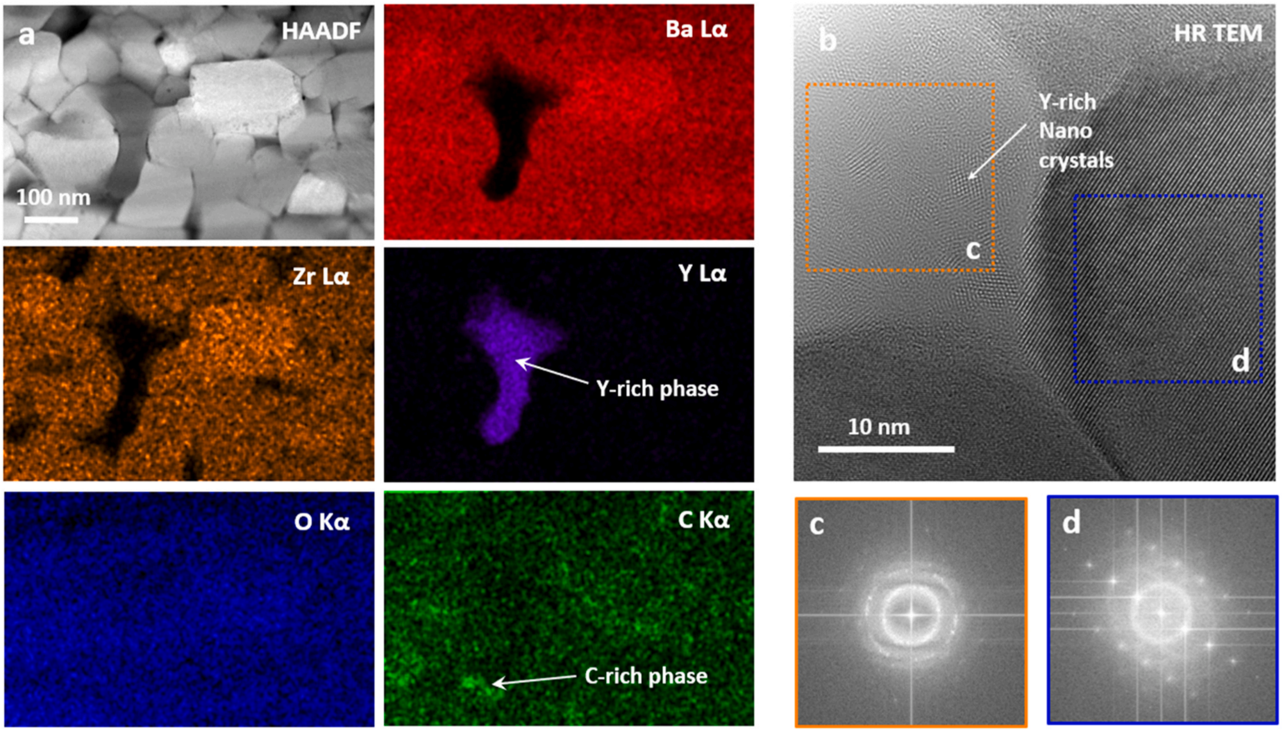

Fig. 9. High resolution (S)TEM imaging of two-step cold sintered BZY20 sintered at 1100 °C. (a) Overview HAADF STEM image and the associated EDS mappings displaying the major components of BZY20 and Carbon (b) Representative HRTEM image of a triple point between two BZY20 grains and a Y-rich secondary phase inclusion. (c, d) Fast Fourier Transformation (FFT) patterns of selected areas from the TEM image in Fig. 8b.

from the decomposition of $Y(OH)_3$ into Y_2O_3. These results confirm the observations that were made using macroscopic characterization techniques.

Additionally, high-resolution transmission electron microscopy (HRTEM) images provide further insights into the nanostructure of a representative interface region between BZY20 grains and the secondary phase (Fig. 9b). Inside the secondary phase, nanometer-sized crystals are embedded within an amorphous matrix. To shed light on the nature of the yttrium-rich secondary phase, a Fast Fourier Transformation (FFT) was conducted on the region corresponding to this phase (highlighted by an orange box). The FFT pattern obtained from this analysis (Fig. 9c) emphasizes the predominantly amorphous nature of the yttrium-rich phase. The absence of well-defined spots in the FFT reveals the lack of long-range order in the yttrium-rich phase, pointing towards an early stage of a recrystallization after the decomposition of volatile phases [53].

For comparison, an additional FFT of the neighboring BZY grain is displayed in Fig. 9d. Here, clear spots are visible highlighting the crystallinity of the selected area. Using STEM and HRTEM characterization, we could reveal the locations of secondary phases inside the microstructure of two-step cold sintered BZY20. Both $BaCO_3$ and Y rich residuals (probably Y_2O_3), which were detected by XRD, can be found predominantly at triple points and as larger side phases inside the grain structure. Particularly the Y-rich secondary phase might facilitate the densification during cold sintering by activating grain sliding and rotation mechanisms. However, due to the unfinished decomposition and re-integration into the perovskite structure, both identified compounds might harm functional properties.

Given that grain boundaries are the most critical feature defining the conductivity of BZY ceramics, the structure and chemical composition of selected interfaces was investigated using high resolution STEM imaging and EDS and is summarized in Fig. 10. The high resolution HAADF image in Fig. 10 a shows a representative grain bounday with the bottom grain aligned along the [100] axis. The high magnification of the HAADF image allows to resolve an intergranular film that is present between both grains (highlighted by dotted lines). The grain boundary film exhibits an inhomogenious, rough appearance and has a thickness of around 1 nm. To elaborate further on the chemical composition, an EDS mapping at the same position is displayed in Fig. 10 b. The alignement of the bottom grain along the [100] axis leads to an intensity difference in the EDS signal, which is induced by channeling effects [54]. This makes high resolution observations only possible on one side of the grain boundary. However, on the aligned side, the major elements Ba and Zr are atomically resolved in the spectral image and a minor Y enrichment can be observed next to the grain boundary. No clear changes are visible in the O and C signal. To get a better comparison of the local elemental disribution, a line scan is derived from the EDS mappings by summarizing the spectral data perpendicular to the grain boundary (Fig, 10c as highlighted by an orange arrow in Fig. 10 b). The Y segregation at the grain boundary is now clearly visible next to the grain boundary core. The increase of Y at the grain boundary is correlated with a simultanious decrease in Zr signal. All other signals are at a constant intensity outside of the center of the grain boundary. The subsitution of Zr with the trivalent Y cation on the B side of the perovskite lattice (ABO_3) is the natural position in a solid solution system like BZY20 [12].

The segregation of negatively charged acceptor dopants towards the charged interface has been observed in several studies for this material system and is driven by the formation of a space charge potential at the grain boundary [55–57]. However, the low extent of cationic segregation which we observe here is not comparable to the pronounced segregation profiles that are present when BZY20 is conventionally processed at high temperatures [25,58]. The low overall sintering temperatures of 1100 °C and the extremely short dwell time of 5 min are preventing a full equilibriation of the cationic composition at the interface, leading to the low extent of segregation and amorphous layers at the grain boundaries.

Similar observations were reported recently for $SrTiO_3$ perovskite ceramics that where reaction-sintered at low temperatures with FAST/SPS [59]. In this system, the segregation of Ti towards the grain boundary is prevented, increasing the specific grain boundary conductivity. However, in the present study, the chemical composition of the grain boundary film, in Fig. 10 a could not be determined. This could be explained by the overall low amount of material at the interface and the possible beam sensitivity of the film. The intergranular film is unstable under long term exposure, which is needed for high resolution EDS mappings (HAADF images before and after the EDS mapping are shown in supplementary Fig. S2).

The extremly low grain boundary conductivity observed in

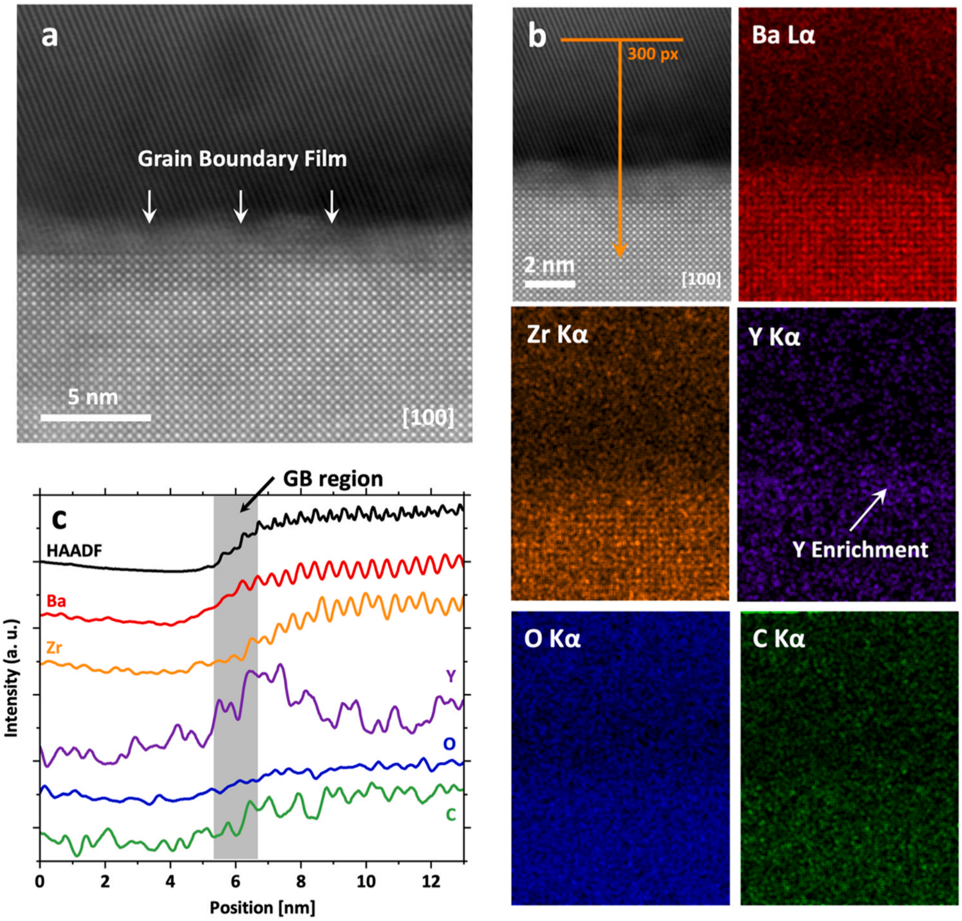

Fig. 10. High resolution STEM-EDS mapping of a grain boundary in two-step cold sintered BZY20. (a) High resolution HAADF STEM image showing an atomically resolved grain boundary between two BZY20 grains (b) HAADF image of the same grain boundary and associated EDS mappings. (c) EDS line scan derived from the EDS maps in (b). The direction and the integration thickness are also visualized in (b).

impedance measurements is likely due to the presence of the intragranular films between BZY grains. Due to a processing window below the decomposition temperature of $BaCO_3$ and an incomplete integration of the Y-rich residues into the perovskite structure, the secondary phases remaining in the microstructure (as intragranular films and secondary phase particles) still represent a detrimental barrier to ionic conductivity.

Future strategies to overcome the limitations posed by secondary phases at the grain boundary might include several pathways: (1) Thermal post-treatments at temperatures high enough to decompose $BaCO_3$ and to intregrate Y residuals into the structure. (2) Optimization of the starting powder composition to reduce the amount of residual $BaCO_3$ while preserving the nanocrystalline powder morphology. (3) Changes of the transient sintering additive chemisty to a $Ba(OH)_2$ hydrated flux or other solid sinterings aids that have been applied in the cold sintering of $BaTiO_3$ [36,60]. However, the processing strategy using a combination of cold sintering and high pressure FAST/SPS presented here allows to strongly reduce the processing temperature and additionally offers various future possibilities to design the sintering behavior and grain boundary properties of barium zirconate based proton conducting ceramics.

4. Conclusions

A new two-step sintering process has been developed for BZY20, enabling cold sintering at 250 °C and stabilization between 900 – 1100 °C inside a FAST/SPS device. The sintering behavior is determined by the Y solution and the formation of $Y(OH)_3$, facilitating densification under high uniaxial pressures. High-resolution characterization and electrochemical testing are made possible by the decomposition of $Y(OH)_3$ during a heat treatment following cold sintering. The resulting BZY20 exhibits a nano-sized microstructure, with residual secondary phases mainly located at grain boundaries and triple points. However, likely amorphous grain boundary films form which significantly reduce the electrochemical performance by a strong reduction of the grain bounday conductivity. Despite the limited conductivity achieved here for BZY20, this innovative approach offers a new pathway for the low-temperature processing of proton-conducting ceramics based on barium zirconate and adds further possibilites to design the grain boundary properties.

CRediT authorship contribution statement

Moritz Kindelmann: Conceptualization, Investigation, Visualization, Writing – original draft, Writing – review & editing. **Julian Ebert:** Investigation, Visualization, Writing – review & editing. **Dylan Jennings:** Investigation, Writing – review & editing. **Doris Sebold:** Investigation, Writing – review & editing. **Wolfgang Rheinheimer:** Resources, Supervision, Funding acquisition, Writing – review & editing. **Martin Bram:** Supervision, Funding acquisition, Writing – review & editing. **Joachim Mayer:** Supervision, Funding acquisition, Project administration, Writing – review & editing. **Olivier Guillon:** Supervision, Funding acquisition, Project administration, Writing – review & editing.

Declaration of Competing Interest

The authors declare that they have no known competing financial interests or personal relationships that could have appeared to influence the work reported in this paper.

Acknowledgement

Walter Sebastian Scheld (IEK-1, Forschungszentrum Jülich) is acknowledged for Raman spectroscopy measurements. M.K is acknowledging the financial support from the DFG in the projects MA 1280/69–1. J. E., D.J. and W.R thank the DFG for funding within the Emmy Noether program (RH 146/1–1).

Appendix A. Supporting information

Supplementary data associated with this article can be found in the online version at doi:10.1016/j.jeurceramsoc.2023.12.060.

References

[1] J.M. Serra, Electrifying chemistry with protonic cells, Nat. Energy 4 (2019) 178–179, https://doi.org/10.1038/s41560-019-0353-y.

[2] L. Yang, S. Wang, K. Blinn, M. Liu, Z. Liu, Z. Cheng, M. Liu, Enhanced sulfur and coking tolerance of a mixed ion conductor for SOFCs: BaZr0.1Ce0.7Y0.2–xYbxO3–d, Sci. (80-.) 326 (2009) 126–129.

[3] C. Duan, J. Tong, M. Shang, S. Nikodemski, M. Sanders, S. Ricote, A. Almansoori, R. O'Hayre, Readily processed protonic ceramic fuel cells with high performance at low temperatures, Sci. (80-.) 349 (2015) 1321–1326, https://doi.org/10.1126/science.aab3987.

[4] C. Duan, R.J. Kee, H. Zhu, C. Karakaya, Y. Chen, S. Ricote, A. Jarry, E.J. Crumlin, D. Hook, R. Braun, N.P. Sullivan, R. O'Hayre, Highly durable, coking and sulfur tolerant, fuel-flexible protonic ceramic fuel cells, Nature 557 (2018) 217–222, https://doi.org/10.1038/s41586-018-0082-6.

[5] S. Choi, C.J. Kucharczyk, Y. Liang, X. Zhang, I. Takeuchi, H.Il Ji, S.M. Haile, Exceptional power density and stability at intermediate temperatures in protonic ceramic fuel cells, Nat. Energy 3 (2018) 202–210, https://doi.org/10.1038/s41560-017-0085-9.

[6] E. Vøllestad, R. Strandbakke, M. Tarach, D. Catalán-Martínez, M.L. Fontaine, D. Beeaff, D.R. Clark, J.M. Serra, T. Norby, Mixed proton and electron conducting double perovskite anodes for stable and efficient tubular proton ceramic electrolysers, Nat. Mater. 18 (2019) 752–759, https://doi.org/10.1038/s41563-019-0388-2.

[7] H. An, H.W. Lee, B.K. Kim, J.W. Son, K.J. Yoon, H. Kim, D. Shin, H. Il Ji, J.H. Lee, A 5 × 5 cm2 protonic ceramic fuel cell with a power density of 1.3 W cm–2 at 600 °C, Nat. Energy 3 (2018) 870–875, https://doi.org/10.1038/s41560-018-0230-0.

[8] V. Kyriakou, I. Garagounis, A. Vourros, E. Vasileiou, A. Manerbino, W.G. Coors, M. Stoukides, Methane steam reforming at low temperatures in a BaZr0.7Ce0.2Y0.1O2.9 proton conducting membrane reactor, Appl. Catal. B Environ. 186 (2016) 1–9, https://doi.org/10.1016/j.apcatb.2015.12.039.

[9] H. Malerød-Fjeld, D. Clark, I. Yuste-Tirados, R. Zanón, D. Catalán-Martinez, D. Beeaff, S.H. Morejudo, P.K. Vestre, T. Norby, R. Haugsrud, J.M. Serra, C. Kjølseth, Thermo-electrochemical production of compressed hydrogen from methane with near-zero energy loss, Nat. Energy 2 (2017) 923–931, https://doi.org/10.1038/s41560-017-0029-4.

[10] C. Daniel, M.-F. Harald, B. Michael, Y.-T. Irene, B. Dustin, A. Simen, N. Kevin, A. Luca, P. Thijs, V.P. K, P.D. K, V.M. I, R.-B. Sonia, N. Truls, B.T. S, S.J. M, K. Christian, S. Aamodt, K. Nguyen, L. Ansaloni, T. Peters, P.K. Vestre, D.K. Pappas, J.M. Serra, C. Kjølseth, Single-step hydrogen production from NH3, CH4, and biogas in stacked proton ceramic reactors, Sci. (80-.) 376 (2022) 390–393, https://doi.org/10.1126/science.abj3951.

[11] D. Ding, Y. Zhang, W. Wu, D. Chen, M. Liu, T. He, A novel low-thermal-budget approach for the co-production of ethylene and hydrogen via the electrochemical non-oxidative deprotonation of ethane, Energy Environ. Sci. 11 (2018) 1710–1716, https://doi.org/10.1039/c8ee00645h.

[12] K.D. Kreuer, Proton-conducting oxides, Annu. Rev. Mater. Res. 33 (2003) 333–359, https://doi.org/10.1146/annurev.matsci.33.022802.091825.

[13] H. Matsumoto, Y. Kawasaki, N. Ito, M. Enoki, T. Ishihara, S. Letters, Relation between electrical conductivity and chemical stability of BaCeO3-based proton conductors with different trivalent dopants, Electrochem. Solid-State Lett. 10 (2007) 2–6, https://doi.org/10.1149/1.2458743.

[14] N. Yan, Y. Zeng, B. Shalchi, W. Wang, T. Gao, G. Rothenberg, J. Luo, Discovery and understanding of the ambient-condition degradation of doped barium cerate proton-conducting perovskite oxide in solid oxide fuel cells, J. Electrochem. Soc. 162 (2015) F1408, https://doi.org/10.1149/2.0371514jes.

[15] K.D. Kreuer, Aspects of the formation and mobility of protonic charge carriers and the stability of perovskite-type oxides, Solid State Ion. 125 (1999) 285–302, https://doi.org/10.1016/S0167-2738(99)00188-5.

[16] P. Babilo, T. Uda, S.M. Haile, Processing of yttrium-doped barium zirconate for high proton conductivity, J. Mater. Res. 22 (2007) 1322–1330, https://doi.org/10.1557/jmr.2007.0163.

[17] Y. Yamazaki, R. Hernandez-Sanchez, S.M. Haile, High total proton conductivity in large-grained yttrium-doped barium zirconate, Chem. Mater. 21 (2009) 2755–2762, https://doi.org/10.1021/cm900208w.

[18] P. Babilo, S.M. Haile, Enhanced sintering of yttrium-doped barium zirconate by addition of ZnO, J. Am. Ceram. Soc. 88 (2005) 2362–2368, https://doi.org/10.1111/j.1551-2916.2005.00449.x.

[19] S. Nikodemski, J. Tong, R. O'Hayre, Solid-state reactive sintering mechanism for proton conducting ceramics, Solid State Ion. 253 (2013) 201–210, https://doi.org/10.1016/j.ssi.2013.09.025.

[20] J. Tong, D. Clark, L. Bernau, A. Subramaniyan, R. O'Hayre, Proton-conducting yttrium-doped barium cerate ceramics synthesized by a cost-effective solid-state reactive sintering method, Solid State Ion. 181 (2010) 1486–1498, https://doi.org/10.1016/j.ssi.2010.08.022.

[21] S. Ricote, N. Bonanos, Enhanced sintering and conductivity study of cobalt or nickel doped solid solution of barium cerate and zirconate, Solid State Ion. 181 (2010) 694–700, https://doi.org/10.1016/j.ssi.2010.04.007.

[22] D. Han, S. Uemura, C. Hiraiwa, M. Majima, T. Uda, Detrimental effect of sintering additives on conducting ceramics: yttrium-doped barium zirconate, ChemSusChem 11 (2018) 4102–4113, https://doi.org/10.1002/cssc.201801837.

[23] K. Ueno, N. Hatada, D. Han, T. Uda, Thermodynamic maximum of y doping level in barium zirconate in co-sintering with NiO, J. Mater. Chem. A. 7 (2019) 7232–7241, https://doi.org/10.1039/c8ta12245h.

[24] Y. Huang, R. Merkle, D. Zhou, W. Sigle, P.A. Van Aken, J. Maier, Effect of Ni on electrical properties of Ba (Zr, Ce, Y) O 3- δ as electrolyte for protonic ceramic fuel cells, Solid State Ion. 390 (2023), 116113, https://doi.org/10.1016/j.ssi.2022.116113.

[25] D.R. Clark, D.R. Diercks, S. Ricote, T. Tauer Dearden, N.P. Sullivan, J.W. Medlin, B. P. Gorman, R.P. O'Hayre, Understanding the effects of fabrication process on BaZr0.9Y0.1O3−δ grain-boundary chemistry using atom probe tomography, J. Mater. Chem. C. 11 (2023) 5082–5091, https://doi.org/10.1039/D2TC04093J.

[26] Y. Huang, R. Merkle, J. Maier, Effects of NiO addition on sintering and proton uptake of Ba(Zr,Ce,Y)O3−δ, J. Mater. Chem. A. 9 (2021) 14775–14785, https://doi.org/10.1039/d1ta02555d.

[27] J. Irvine, J.L.M. Rupp, G. Liu, X. Xu, S. Haile, X. Qian, A. Snyder, R. Freer, D. Ekren, S. Skinner, O. Celikbilek, S. Chen, S. Tao, T.H. Shin, R. O'Hayre, J. Huang, C. Duan, M. Papac, S. Li, V. Celorrio, A. Russell, B. Hayden, H. Nolan, X. Huang, G. Wang, I. Metcalfe, D. Neagu, S.G. Martín, Roadmap on inorganic perovskites for energy applications, JPhys Energy 3 (2021), https://doi.org/10.1088/2515-7655/abff18.

[28] M.C. Tucker, Progress in metal-supported solid oxide electrolysis cells: a review, Int. J. Hydrog. Energy 45 (2020) 24203–24218, https://doi.org/10.1016/j.ijhydene.2020.06.300.

[29] N. Sata, F. Han, H. Zheng, A.M. Dayaghi, T. Norby, M. Stange, R. Semerad, R. Costa, Development of proton conducting ceramic cells in metal supported architecture, 95–95, ECS Meet. Abstr. MA2021-03 (2021), https://doi.org/10.1149/ma2021-03195mtgabs.

[30] M. Bram, N.H. Menzler, Metal-supported cells, High. -Temp. Electro (2023) 8–26, https://doi.org/10.1088/978-0-7503-3951-3ch8.

[31] J. Guo, H. Guo, A.L. Baker, M.T. Lanagan, E.R. Kupp, G.L. Messing, C.A. Randall, Cold sintering: a paradigm shift for processing and integration of ceramics, Angew. Chem. Int Ed. Engl. 55 (2016) 11457–11461, https://doi.org/10.1002/anie.201605443.

[32] M.Y. Sengul, J. Guo, C.A. Randall, A.C.T. van Duin, Water-mediated surface diffusion mechanism enables the cold sintering process: a combined computational and experimental study, Angew. Chem. Int. Ed. 58 (2019) 12420–12424, https://doi.org/10.1002/anie.201904738.

[33] B. Dargatz, J. Gonzalez-Julian, O. Guillon, Improved compaction of ZnO nano-powder triggered by the presence of acetate and its effect on sintering, Sci. Technol. Adv. Mater. 16 (2015) 25008, https://doi.org/10.1088/1468-6996/16/2/025008.

[34] S. Funahashi, J. Guo, H. Guo, K. Wang, A.L. Baker, K. Shiratsuyu, C.A. Randall, Demonstration of the cold sintering process study for the densification and grain growth of ZnO ceramics, J. Am. Ceram. Soc. 100 (2017) 546–553, https://doi.org/10.1111/jace.14617.

[35] K. Nur, T.P. Mishra, J.G.P. da Silva, J. Gonzalez-Julian, M. Bram, O. Guillon, Influence of powder characteristics on cold sintering of nano-sized ZnO with density above 99%, J. Eur. Ceram. Soc. 41 (2021) 2648–2662, https://doi.org/10.1016/j.jeurceramsoc.2020.11.007.

[36] K. Tsuji, A. Ndayishimiye, S. Lowum, R. Floyd, K. Wang, M. Wetherington, J.-P. Maria, C.A. Randall, Single step densification of high permittivity BaTiO3 ceramics at 300 °C, J. Eur. Ceram. Soc. 40 (2020) 1280–1284, https://doi.org/10.1016/j.jeurceramsoc.2019.12.022.

[37] N. Guo, H.-Z. Shen, P. Shen, One-step synthesis and densification of BaTiO3 by reactive cold sintering, Scr. Mater. 213 (2022), 114628, https://doi.org/10.1016/j.scriptamat.2022.114628.

[38] T.H. Zaengle, A. Ndayishimiye, K. Tsuji, Z. Fan, S.H. Bang, J. Perini, S.T. Misture, C.A. Randall, Single-step densification of nanocrystalline CeO2 by the cold sintering process, J. Am. Ceram. Soc. 103 (2020) 2979–2985, https://doi.org/10.1111/jace.17003.

[39] A. Kabir, M. Espineira-Cachaza, E.M. Fiordaliso, D. Ke, S. Grasso, B. Merle, V. Esposito, Effect of cold sintering process (CSP) on the electro-chemo-mechanical properties of Gd-doped ceria (GDC), J. Eur. Ceram. Soc. 40 (2020) 5612–5618, https://doi.org/10.1016/j.jeurceramsoc.2020.06.010.

[40] S. Ohta, M. Kawakami, H. Nozaki, C. Yada, T. Saito, H. Iba, Li+ conducting garnet-type oxide sintering triggered by an H+/Li+ ion-exchange reaction, J. Mater. Chem. A. 8 (2020) 8989–8996, https://doi.org/10.1039/D0TA00059K.

[41] J.-H. Seo, H. Nakaya, Y. Takeuchi, Z. Fan, H. Hikosaka, R. Rajagopalan, E. D. Gomez, M. Iwasaki, C.A. Randall, Broad temperature dependence, high conductivity, and structure-property relations of cold sintering of LLZO-based composite electrolytes, J. Eur. Ceram. Soc. 40 (2020) 6241–6248, https://doi.org/10.1016/j.jeurceramsoc.2020.06.050.

[42] M. Kindelmann, J.N. Ebert, W.S. Scheld, W. Deibert, W.A. Meulenberg, W. Rheinheimer, M. Bram, J. Mayer, O. Guillon, Cold sintering of BaZr0.7Ce0.2Y0.1O3-δ ceramics by controlling the phase composition of the starting powders, Scr. Mater. 224 (2023), 115147, https://doi.org/10.1016/j.scriptamat.2022.115147.

[43] M. Kindelmann, S. Escolastico, L. Almar, A. Vayyala, D. Jennings, J. Mayer, O. Guillon, Highly conductive grain boundaries in cold-sintered barium zirconate based proton conductors, (2023).

[44] J.N. Ebert, D. Jennings, L.-A. Schäfer, D. Sebold, W. Rheinheimer, Bulk and grain boundary conductivity in doped BaZrO3: bulk contribution dominates at operating temperatures, Scr. Mater. 241 (2024) 0–5, https://doi.org/10.1016/j.scriptamat.2023.115852.

[45] D. Jennings, J.N. Ebert, H. Du, Q. Ma, L. Sch, D. Sebold, J. Mayer, W. Rheinheimer, The formation of stacking faults in barium zirconate-type perovskites, Chem. Mater. (2023), https://doi.org/10.1021/acs.chemmater.3c00787.

[46] J.E. Bauerle, Study of solid electrolyte polarization by a complex admittance method, J. Phys. Chem. Solids 30 (1969) 2657–2670, https://doi.org/10.1016/0022-3697(69)90039-0.

[47] J.T.S. Irvine, D.C. Sinclair, A.R. West, Electroceramics: characterization by impedance spectroscopy, Adv. Mater. 2 (1990) 132–138.

[48] J.G. Lyagaeva, G.K. Vdovin, D.A. Medvedev, Distinguishing bulk and grain boundary transport of a proton-conducting electrolyte by combining equivalent circuit scheme and distribution of relaxation times analyses, J. Phys. Chem. C. 123 (2019) 21993–21997, https://doi.org/10.1021/acs.jpcc.9b05705.

[49] M. Ghaderi, R.S. Razavi, M.R. Loghman-estarki, S. Ghorbani, Spark plasma sintering of transparent Y2O3 ceramic using hydrothermal synthesized nanopowders, Ceram. Int. (2016) 1–8, https://doi.org/10.1016/j.ceramint.2016.06.022.

[50] D. Lee, J.-A. Lee, Y.-W. Heo, J.-H. Lee, J.-I. Jung, J.-J. Kim, The effect of yttrium nitrate addition on the densification behaviour of Y2O3 ceramics during the cold sintering process, J. Eur. Ceram. Soc. 40 (2020) 3208–3214, https://doi.org/10.1016/j.jeurceramsoc.2020.02.025.

[51] I. Arvanitidis, D. Siche, S. Seetharaman, A study of the thermal decomposition of BaCO3, Metall. Mater. Trans. B. 27 (1996) 409–416, https://doi.org/10.1007/BF02914905.

[52] J.N. Ebert, D. Jennings, L.-A. Schäfer, D. Sebold, W. Rheinheimer, Bulk and grain boundary conductivity in doped BaZrO3: Bulk contribution dominates at operating temperatures, Scr. Mater. (2023).

[53] S.H. Bang, M.Y. Sengul, Z. Fan, A. Ndayishimiye, A.C.T. van Duin, C.A. Randall, Morphological and chemical evolution of transient interfaces during zinc oxide cold sintering process, Mater. Today Chem. 24 (2022), 100925, https://doi.org/10.1016/j.mtchem.2022.100925.

[54] B. Feng, N.R. Lugg, A. Kumamoto, N. Shibata, Y. Ikuhara, On the quantitativeness of grain boundary chemistry using STEM EDS: A ZrO2 Σ9 model grain boundary case study, Ultramicroscopy 193 (2018) 33–38, https://doi.org/10.1016/j.ultramic.2018.05.010.

[55] M. Shirpour, B. Rahmati, W. Sigle, P.A. Van Aken, R. Merkle, J. Maier, Dopant segregation and space charge effects in proton-conducting BaZrO 3 perovskites, J. Phys. Chem. C. 116 (2012) 2453–2461, https://doi.org/10.1021/jp208213x.

[56] M. Shirpour, G. Gregori, L. Houben, R. Merkle, J. Maier, High spatially resolved cation concentration profile at the grain boundaries of Sc-doped BaZrO3, Solid State Ion. 262 (2014) 860–864, https://doi.org/10.1016/j.ssi.2013.11.032.

[57] A. Lindman, T.S. Bjørheim, G. Wahnström, Defect segregation to grain boundaries in BaZrO3 from first-principles free energy calculations, J. Mater. Chem. A. 5 (2017) 13421–13429, https://doi.org/10.1039/c7ta01080j.

[58] D.R. Clark, H. Zhu, D.R. Diercks, S. Ricote, R.J. Kee, A. Almansoori, B.P. Gorman, R.P. O'Hayre, Probing grain-boundary chemistry and electronic structure in proton-conducting oxides by atom probe tomography, Nano Lett. 16 (2016) 6924–6930, https://doi.org/10.1021/acs.nanolett.6b02918.

[59] M.P. Zahler, D. Jennings, M. Kindelmann, O. Guillon, W. Rheinheimer, Reactive FAST/SPS sintering of strontium titanate as a tool for grain boundary engineering, J. Eur. Ceram. Soc. (2023), https://doi.org/10.1016/j.jeurceramsoc.2023.07.021.

[60] T. Sada, K. Tsuji, A. Ndayishimiye, Z. Fan, Y. Fujioka, C.A. Randall, High permittivity BaTiO3 and BaTiO3-polymer nanocomposites enabled by cold sintering with a new transient chemistry: Ba(OH)2•8H2O, J. Eur. Ceram. Soc. 41 (2021) 409–417, https://doi.org/10.1016/j.jeurceramsoc.2020.07.070.